Recent experiments in the EAST and HT-7 superconducting tokamaks

To cite this article: Baonian Wanfor the EAST and HT-7 Teams and International Collaborators 2009 *Nucl. Fusion* **49** 104011

IOP Publishing and International Atomic Energy Agency — Nuclear Fusion
Nucl. Fusion **49** (2009) 104011 (15pp) doi:10.1088/0029-5515/49/10/104011

Recent experiments in the EAST and HT-7 superconducting tokamaks

Baonian Wan[a] **for the EAST and HT-7 Teams and International Collaborators**[b]

Institute of Plasma Physics, Chinese Academy of Sciences, Hefei, People's Republic of China

E-mail: bnwan@ipp.ac.cn

Received 28 November 2008, accepted for publication 17 June 2009
Published 9 September 2009
Online at stacks.iop.org/NF/49/104011

Abstract
First divertor plasma configuration in Experimental Advanced Superconducting Tokamak (EAST) was obtained in the second campaign after the last IAEA meeting. To achieve long pulse diverted plasma discharges, new capabilities including the fully actively water cooled in-vessel components, current drive and heating systems, diagnostics and real-time plasma control algorithm were developed. Pre-programmed shape and feedback control of plasma position and current (RZIP) produced a variety of shaped plasma configurations, covering most of the configurations foreseen at the design stage of the machine. Control algorithm based on real-time equilibrium reconstruction and iso-flux control for the last closed magnetic flux surface (RTEFIT/ISOFLUX) has also been realized. A number of operational issues, such as plasma initiation and ramp up under constraints of superconducting coils were successfully investigated. First LHCD experiments demonstrated long pulse discharges longer than 20 s and nearly full non-inductive current drive. The physical engineering capability on the superconducting magnetic system was assessed by simulating discharges. Since the last IAEA meeting, experiments in HT-7 have been focusing on long pulse operation to support the EAST experiments on both physics and technical aspects. Long pulse discharges up to 400 s have now been achieved in HT-7. Investigation of sawtooth activities in ohmic and LHCD plasmas supports the turbulence model instead of the fast reconnection of the $m = 1$ magnetic island. Coexistence of electron mode and ion mode in high density ohmic plasmas has been observed by 2D ECE imaging (ECEI) in HT-7. The spectral characteristics of geodesic acoustic mode at the plasma boundary have been investigated by Langmuir probe arrays.

PACS numbers: 52.50, 52.55

(Some figures in this article are in colour only in the electronic version)

1. Introduction

Experimental Advanced Superconducting Tokamak (EAST) engineering construction has been successfully completed [1, 2], with the first divertor plasma configuration being achieved in the second campaign right after the last IAEA meeting. Fully superconducting coils and strongly shaped plasma configurations are required for future tokamak fusion power plants. EAST is presently the only such tokamak in the world that can address both issues simultaneously.

EAST has actively cooled plasma facing components (PFCs). It is equipped with a 2 MW lower hybrid current drive (LHCD) system and a 1.5 MW ion cyclotron resonant heating (ICRH) system. The radio frequency (RF) heating and current drive systems will be extended to 8–10 MW in the next 2 years and a 4 MW neutral beam injection system is expected to be available in 3–4 years. These capabilities make EAST a unique facility to explore some of the critical issues relating to steady-state operation with shaped plasma cross-section in the next few years. It could become a good test bed, in particular, for the technology of steady-state divertor control and physics of long pulse operation with non-inductive current drive, and provide operational experience of a full superconducting machine.

The Institute of Plasma Physics, Chinese Academy of Sciences (IPP/CAS or ASIPP) has both newly built EAST and HT-7 superconducting tokamak in operation. Significant progress has been achieved in EAST construction/operation and HT-7 experiments with many contributions from broad international collaboration. In the last two years, HT-7 experiments were strongly oriented to support the EAST project both physically and technically [3, 4]. HT-7 is used for specific physics investigation, in particular long pulse discharges, edge plasma turbulence, etc. Experience and experimental achievements from the HT-7 operation have

[a] Author to whom any correspondence should be addressed.
[b] See the appendix.

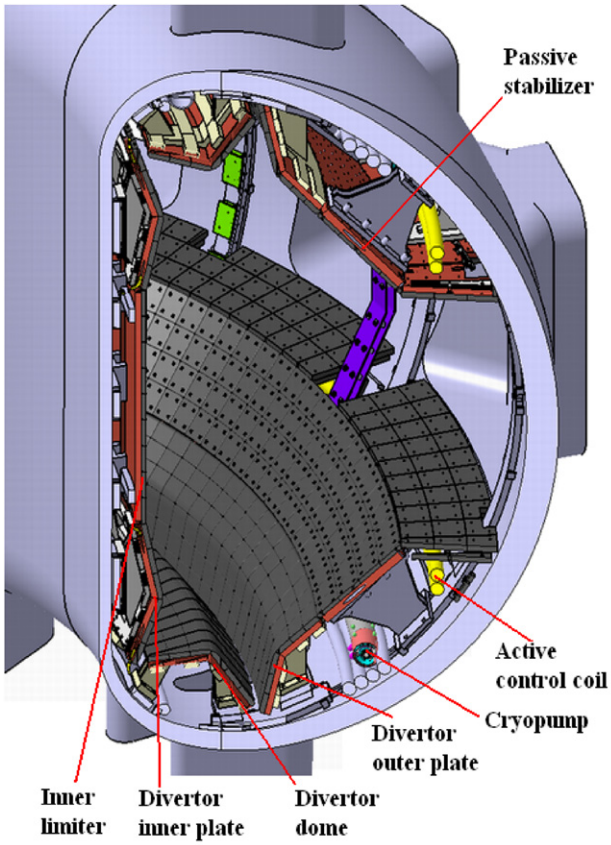

Figure 1. Elevation view of EAST in-vessel structure.

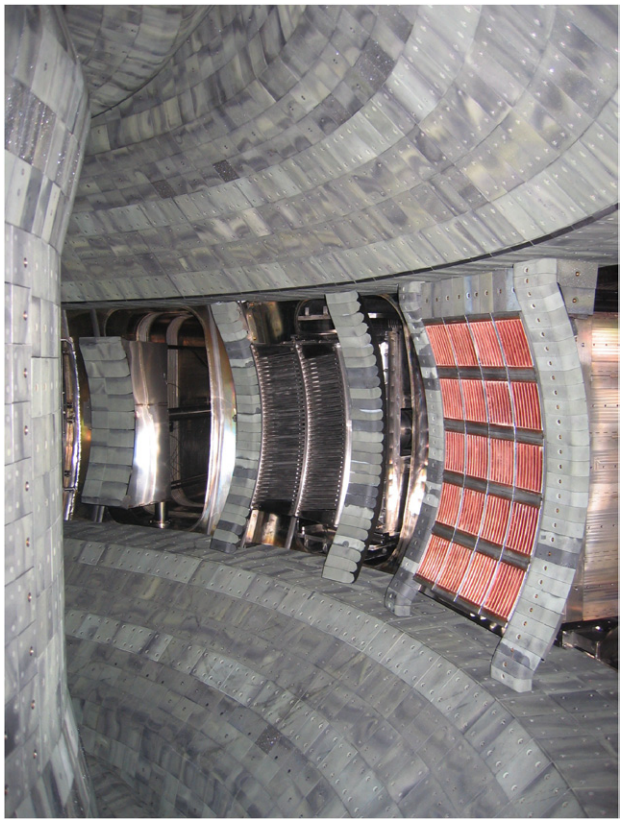

Figure 2. Picture of in-vessel together with the ICRF antenna and LHCD launcher. From right to left of the figure, the elements are LHCD launcher, ICRF antenna and movable limiter.

become an important part of the EAST basis and contributed to speeding up EAST start-up.

This paper will report the main progress of machine modification and operation on EAST and long pulse experiments on HT-7. It is organized as follows: section 2 briefly describes the recent upgrade on EAST, mainly, the new in-vessel structure. The experimental progress on EAST with the new in-vessel structure is given in section 3. Results from long pulse operation in HT-7 are reported in section 4, followed by a summary and near future plan in section 5.

2. System development on EAST

The first EAST plasma was achieved under the full metal PFCs condition [2]. EAST, as a full superconducting tokamak, is aimed at long pulse (60–1000 s) high performance operation, which requires specific in-vessel structures and PFCs. It should be capable of handling particle and heat fluxes through the plasma boundary to the wall in a variety of operation scenarios under steady-state conditions, as well as protecting vacuum vessel and other components such as magnetic sensors and internal cryopump, from direct plasma interaction. The in-vessel structure is a complicated integration of multi-systems as shown in figure 1, including fully actively water cooled PFCs and supporting structures, a full set of magnetic inductive sensors for machine operation and plasma control, divertor cryopump, actively water cooled internal coils for vertical stabilization control, divertor probe arrays, baking system and thermal coupler, etc. All these elements are newly built, except the internal coils, since the first plasma with full metal PFCs was achieved [2]. The system of the actively cooled PFC is a key element in the construction of the new in-vessel structure. Figure 2 shows the EAST in-vessel structure together with ICRF antenna and LHCD launcher. The geometry is designed for top–bottom symmetry to accommodate both double null and single null divertor configurations. This section only gives a very brief summary of the newly developed systems on EAST. Details of each system will be described in separate papers.

2.1. Plasma facing components

In the first phase (2008–2011) of EAST operation, total heating and current drive power will be about 8–10 MW. The peak heat flux on the divertor plates will be under 3.6 MW m^{-2} , based on the B2-Eirene simulation for typical EAST operation scenarios with line-averaged density greater than 2×10^{19} m^{-3}. From economical and technical considerations, bolted tiles rather than brazed tiles are used in the initial phase of the PFCs engineering design. The PFCs consist of a plasma facing surface attached to an actively cooled heat sink. All plasma facing surfaces are made of multi-element doped graphite materials [5]. The 15 mm or 20 mm (especially for divertor) thick graphite tiles are bolted to a copper alloy (CuCrZr) heat sink and restrained through spring washers that allow limited deformation during thermal expansion. This mechanically restrained structure is used for all PFCs. The thermal conductance across the tile to heat sink interface is very

important for the performance of bolted tiles. A thin graphite sheet of 0.38 mm is used between the tile and the heat sink to improve thermal contact. The bolted structure should provide a minimum of 0.2 MPa average pressure over the contact area. Water-cooling channels consist of drilled holes directly along the 20 mm thick heat sink plates. Such a structure, with a $2\,\mathrm{t\,h^{-1}}$ water mass flow rate for inner target, outer target and dome, can maintain plasma facing surface temperature around 800 °C under peak heat load up to $3.6\,\mathrm{MW\,m^{-2}}$ according to the thermo-hydraulic analysis.

Each of the upper and lower divertor structures consists of three high heat flux targets: inner, outer and private baffle (dome) plates. The vertical targets and dome form a 'V' shape, where particles distribute heat load uniformly on the divertor plates. Two gaps between inner, outer targets and dome were provided with a total of $180\,\mathrm{m^3\,s^{-1}}$ gas conductance for particle and impurity exhaust by cryopump. Other PFCs except the divertor region have the same structure but with lower cooling capability, which allow a maximum heat load of $0.5\,\mathrm{MW\,m^{-2}}$. A passive stabilizer is placed on the outer board region above and below the mid-plane. The thickness of the stabilizer is 30 mm copper alloy with carbon tiles for protection and coolant channels for cooling. All PFCs were divided into 16 modules in the toroidal direction. They can be placed into and removed from the vacuum vessel through horizontal ports to facilitate maintenance and handling. The PFCs modules have some flexibility relative to the vacuum vessel in order to reduce the magnitude of the differential thermal expansion loads that can occur during both operation and baking. In the present status, the passive stabilizers on each module are independent of each other. They can be electrically connected at a later time when sufficient experience of the in-vessel structure is gained from operation and no significant modification is needed. Halo current is considered to be 50% of plasma current with a toroidal asymmetry factor of 2 in the design.

Two movable molybdenum limiters have been installed, which allow radial displacement from 2.26 to 2.42 m.

2.2. *In-vessel coils and cryopump*

The poloidal field (PF) coils are normally quite far from the plasma in a fully superconducting machine, to ensure relatively weak coupling between the PF coils and the plasma. On the other hand, the current variation rates in the superconducting PF coils are limited due to ac losses, which affect the stability of the magnets. EAST vacuum chamber wall is relatively far from the plasma for typical plasma configurations, due to the presence of fully active cooled in-vessel components, which results in a relative weak vertical stabilization. These lead to insufficient capability of stabilizing highly shaped plasma. In-vessel coils close to plasma with fast power supplies are utilized as a solution for vertical stabilization, as also shown in figure 1. The coils have been actively water cooled and can be operated at a current up to 20 kA/turn under steady-state conditions. The corresponding power supply is operated in the current-control mode with a temporal response of 100 μs. Present modules can provide a maximum current of 5 kA. The extension of power supply capability by adding more modules is planned.

A cryopump is installed behind the first wall and diverter plates, fixed to the vacuum vessel wall, to avoid facing the plasma directly, as shown in figure 1. The cryopump is located in the plenum under the outer diverter plate and the passive stabilizer, near the gap between the dome target and the outer target, providing a pumping speed $>15\,\mathrm{m^3\,s^{-1}}$. The pump consists of continuous tubes with pumping slot open to the vacuum vessel wall, which are supported by flexible supports (figure 3).

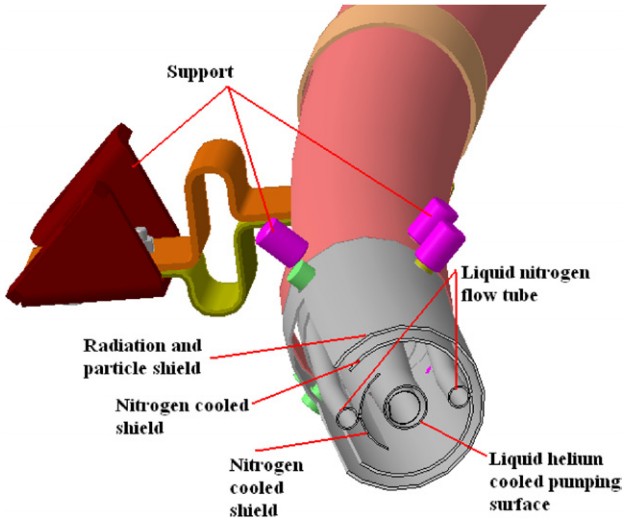

Figure 3. Elevation view of EAST toroidally continuous cryopump.

2.3. *Wall conditioning*

EAST vacuum chamber has a double layer structure. It can be baked up to 250 °C by high pressure hot nitrogen gas, provided by a gas heater, via regulation of the temperature and the flow rate of the heating gas. The PFCs can also be baked by hot nitrogen gas flowing in the cooling lines of the heat sinks. They can be baked up to 350 °C before water cooling is applied. Four dc glow discharge anodes and two RF conditioning antennas have been installed for wall conditioning. These two RF antennas are fed by a RF power generator of 24–30 MHz and 10–100 kW in CW mode. RF conditioning is normally used for boronization and wall cleaning, and, in some cases, is also applied during breakdown as pre-ionization in pulsed mode. The thermal couples are attached to the chamber and port extension walls and embedded in the graphite tiles of the liner, limiter and divertor for wall conditioning, as well as plasma discharges.

2.4. *Diagnostics*

All magnetic sensors are newly manufactured and have been installed in the vacuum chamber as an integral part of the in-vessel components. Magnetic measurements consist of three Rogowskii coils in the vacuum chamber for plasma current and two outside the vessel for vessel current, 2×37 flux loops, 3×39 probe arrays, two Mirnov coil arrays along the poloidal direction and a 20 coil array in the toroidal direction, two sets of diamagnetic and compensation coils, eight Rogowskii coils surrounding the support legs for halo current, four sets of poloidal saddle coils arrays symmetrically located at four toroidal positions. These magnetic sensors

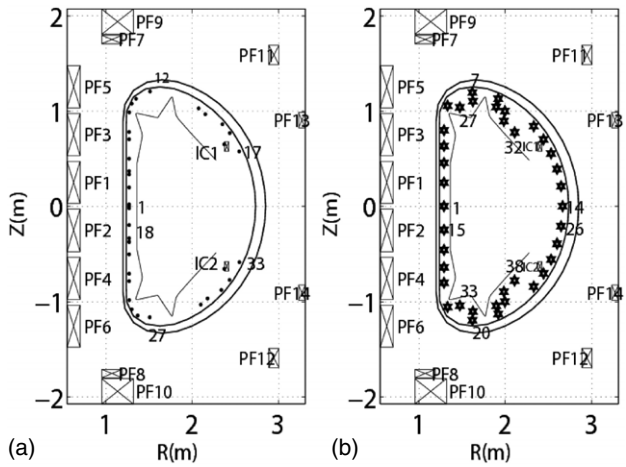

Figure 4. (*a*) Poloidal distribution of flux loops and (*b*) poloidal distribution of magnetic probes.

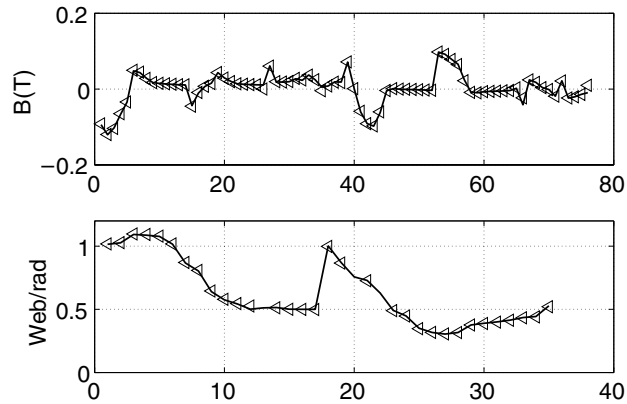

Figure 5. A comparison of measurement (triangle points) and calculation (line) by exciting the PF coils. Top plot is from magnetic probes and bottom from flux loops.

provide sufficient information for machine operation, plasma control and physics analysis. The distribution of flux loops and magnetic probes along the poloidal direction is shown in figure 4. All magnetic sensors are carefully positioned and calibrated with the newly developed low-drift integrator to ensure the accuracy needed for plasma equilibrium reconstruction. Uncertainties of most magnetic probes and flux loops are less than 10 G and 2%, respectively, which are better than the designed specifications. An example of the testing result is shown in figure 5, which gives a comparison of the measurement (triangle points) and the calculation (line) by exciting the PF coils.

Two Langmuir probe and Mach probe arrays were designed as an important integral part of the specific diverter and dome modules. They were made by graphite rods and cooled through thermal conducting to the heat sink of the modules, which are actively water cooled. The probes were mounted on the top and the bottom diverter plates, as well as the dome. Individual probe tips can be easily configured as triple probe arrays along the divertor plates with a poloidal resolution of 2 cm. The Mach probe consists of four tips, which are oriented for the toroidal and poloidal velocity measurements.

An advanced x-ray imaging crystal spectrometer (XCS), developed in collaboration with PPPL and NFRI, has been

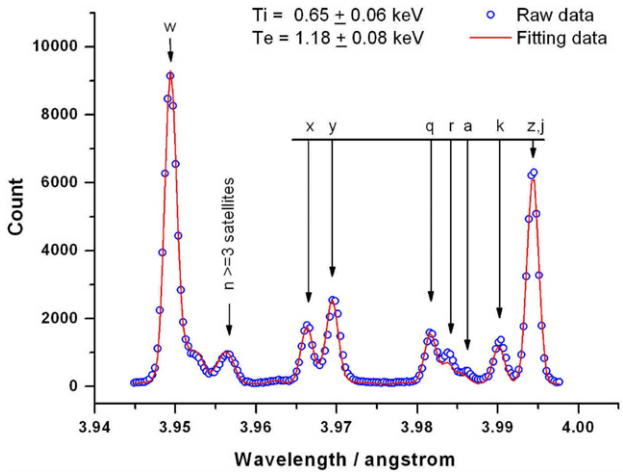

Figure 6. A helium-like argon spectrum taken from the central sight line.

installed at the end of the main pumping duct of EAST. The advanced XCS, which can be used to record both temporally and spatially resolved spectra of helium-like ions from multiple sightlines through the plasma, is a powerful diagnostic for the measurement of ion and electron temperature profiles in tokamak plasmas [6]. Figure 6 gives an example of the helium-like argon spectrum taken from the central chord by puffing Ar gas as seed impurity into an ohmic plasma on EAST. The fitting curve and derived ion and electron temperatures are also shown in the figure. The XCS consists of a spherically bent crystal and a large area, segmented 2D position-sensitive multiwire proportional counter [7]. The XCS is presently the only diagnostics that can provide ion and electron temperatures simultaneously on EAST.

There is a single channel laser interferometer with the vertical sight line at $R = 1.9$ m, which provides line integrated density measurements and is also used for density feedback control. Two visible CCD cameras view the plasma in tangential sight line to monitor plasma discharges. Additional 20 diagnostics presently installed can provide the measurements of electron temperatures, surface temperatures of the liner or diverter plates, radiation power and information from soft-x rays, visible to near UV impurity radiation, h_α radiation, etc. Hard-x ray and neutron flux measurements are also available for LHCD experiments and to monitor runaway electrons.

2.5. *Plasma control system*

Plasma discharges are controlled by a plasma control system (PCS) built in collaboration with GA, which is similar to the PCS of DIII-D, but with new EAST features such as the coil current ramping rate limitations due to the eddy current heating on the superconducting cables and the IC power supply command algorithms [8].

2.6. *RF systems*

The RF systems with maximum output powers of 1.5 MW in the ion cyclotron resonant frequency range 30–110 MHZ and 2 MW in the lower hybrid frequency range at 2.45 GHz

are available for heating and current drive, as well as wall conditioning and discharge pre-ionization. A resonant double loop antenna with two straps was designed for ICRF heating and current drive in collaboration with the Tore Supra teams in France. The key elements of this antenna are actively water cooled to accommodate requirements for long pulse operation. Two current straps can be powered with different phasings for heating and current drive, which provides capabilities for various operation scenarios. The LHCD system is similar to the system used in HT-7 [9]. It consists of twenty klystron amplifiers, which can each deliver 100 kW with CW capacity at 2.45 GHz. A multi-junction coupler consists of 5 column × 4 row main waveguides. Each main waveguide is split into eight sub-waveguides and powered by individual klystron amplifiers. The coupler can launch the LHCD power with parallel refractive index $N_\parallel$ of 1.6–3.2 and typical FWHM of 0.2 at $N_\parallel^{\mathrm{peak}} = 2.3$. The spectrum of $N_\parallel$ can be changed within a fast response time of 0.1 ms during one discharge, which provides a possible tool for the control of the plasma current density profile.

3. The first experiments with new PFCs

EAST, as a full superconducting tokamak, faces new challenges, as compared with conventional tokamaks and those only with toroidal superconducting coils. These issues, particularly, the limitation of current ramping rate in PF coils, relatively weak coupling between plasma and PF coils, PF field penetration through the vacuum vessel and thermal shielding from the plasma, etc, which affect machine operation, have been discussed briefly in [2]. The key issue is to reduce the current variation rate by optimizing plasma operation scenarios, particularly during the plasma current buildup phase, which is important for the stability and safety of superconducting magnets with fixed cooling capability under steady-state conditions.

The graphite tiles and the vacuum chamber wall were baked up to nearly 300 °C and 200 °C, respectively, continuously for about 10 days before plasma discharges. However, the burn through mainly due to out-gassing from the graphite tiles still causes difficulty for further current ramping up after breakdown. To achieve reliable breakdown and plasma current ramping up, RF cleaning and boronization are used as routine wall conditioning techniques on EAST. The working gas was hydrogen in 2007 and switched to deuterium for the recent campaign in 2008.

3.1. Plasma shaping and control

The experiments were initiated using pre-programming shape control and feedback control for plasma position and current (RZIP control algorithm) with the internal control coils (ICs) for vertical stabilization. The principal goal of this experiment was to achieve stably controlled shape and position of diverted plasmas with sufficient elongations up to 1.9 and triangularities up to 0.64. To verify the shaping capabilities of the poloidal field system and the vertical stabilization of ICs, highly shaped plasmas for various configurations have been stably produced. The results are summarized in figure 7 for the campaigns in 2007 with full metal wall and 2008 with the new PFCs,

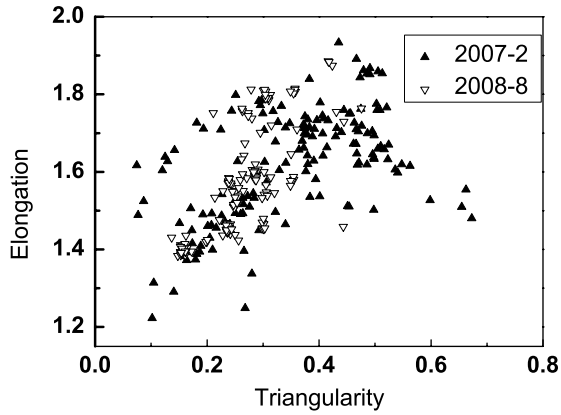

Figure 7. Operation space for highly shaped plasma discharges.

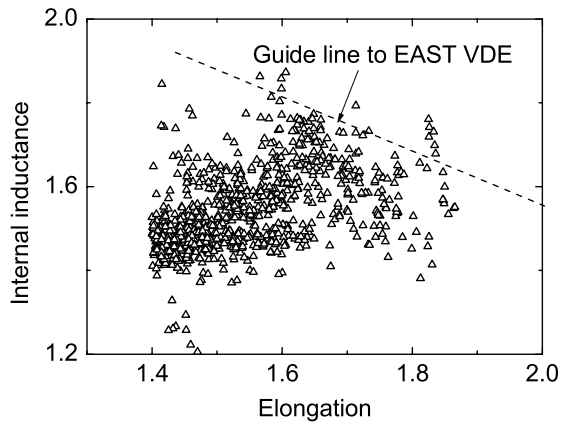

Figure 8. Operation space for vertical stability.

which are obtained with the full equilibrium reconstruction of both EFIT(GA) [10] and IPPEQ(ASIPP). The relation between elongation and internal inductance for well stabilized and shaped plasmas is given in figure 8. The following configurations have been produced and stably controlled for both shape and position of plasmas: double null configuration with elongation kappa = 1.9 and triangularity delta = 0.50; top or bottom single null configurations with kappa = 1.7 and delta = 0.64 with a plasma current up to 0.6 MA. The above results cover most configurations foreseen at the design stage of the machine and confirm the capabilities of the poloidal field systems including ICs and their power supplies for the present operation regimes. Discharges with plasma current ranged from 0.2 to 0.6 MA and the toroidal magnetic field from 2 to 3 T show the confinement roughly consistent with Neo-Alcator scaling in the linear ohmic confinement (LOC) regime and saturated at about 100 ms for ohmic plasmas shown in figure 9. Most of these data were obtained at plasma current between 250–300 kA and B_t ∼2 T in the circular and elongated limiter configurations. Note that the dataset shown in figure 9 is rather scattered. The main reason may be that the confinement in the elongated and diverted configurations could differ from the Neo-Alcator scaling as reported from other machines. In addition, the effective charge number Z_{eff} may affect the confinement [11]. However, present observations of ohmic plasmas are not sufficient to perform a more detailed analysis as done in other machines, which is left as future work. The LOC

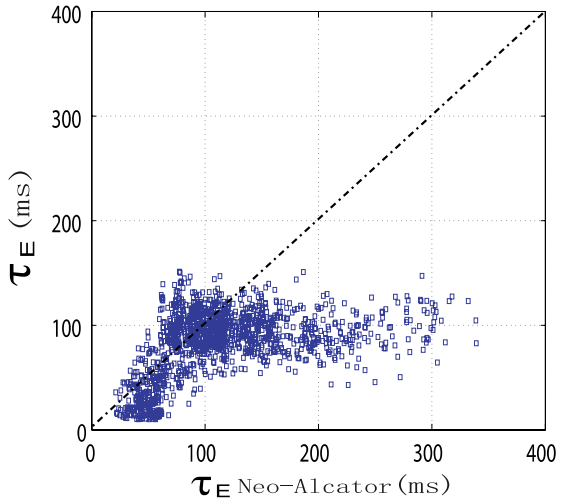

Figure 9. Confinement scaling for ohmic plasma discharges and comparison with Neo-Alcator scaling. Confinement time is saturated at about 100 ms and density higher than $1.5 \times 10^{19}\,\mathrm{m}^{-3}$.

regime shown in figure 9 is clearly identified with saturation density $n_{\mathrm{sat}} \sim 1.5 \times 10^{19}\,\mathrm{m}^{-3}$, as can be deduced in a density scaling experiment under the conditions of $I_{\mathrm{p}} \sim 250$ kA and $B_{\mathrm{t}} \sim 2$ T in the circular and elongated (up to 1.5) limiter configurations. This confinement comparable to the Neo-Alcator scaling in the LOC regime implies an acceptable level of impurity particle in plasmas with the new PFCs, although present diagnostics cannot provide direct Z_{eff} measurements. Such experiments provide the basis for algorithm development and optimization of real-time plasma shape control.

Advanced steady-state tokamak plasma operation relies on the exact control of the plasma shape and positions in order to improve the coupling of heating and current drive by RF waves, and protect the divertor by the accurate control of the striking points, etc. The full reconstruction of the equilibrium has been performed by using the EFIT [10] code routinely between shots. This kind of reconstruction was made to be real-time (RTEFIT) and sufficiently fast for the real-time shape control in DIII-D by using fast loop and slow loop calculations on separate CPUs. While RTEFIT has been done during a control cycle, the control reference points, which were derived from the shape of the last closed magnetic flux surface, were determined first. The flux difference between measured and pre-defined values at the reference points was controlled to be zero based on the so-called RTEFIT/ISOFLUX algorithm, which was first realized in DIII-D [12]. Under collaboration with the DIII-D team, EAST also adapted the DIII-D plasma control software system [8]. The RTEFIT/ISOFLUX control algorithm was primarily realized on EAST in the 2008 campaign shown in figure 10. The control points are shown as cross symbols, together with the plasma shape and flux surfaces, as shown on the right of figure 10. The uppermost and lowest points are the top and bottom X points, respectively. The other points in the figure were chosen in such a way as to mainly control the inner gap by the innermost point, outer gap by the outmost point and the upper and lower triangularities by the other points. Figure 11 shows the flux errors at mid-plane outboard and inboard control points for the isoflux control algorithm. It can be seen that the flux errors were well controlled below 5 mV s for most of the discharge time under shape control which started from 3 s. The right of figure 10 gives the plasma configuration at several time slices after the isoflux control algorithm was applied. The X point is stably controlled with position fluctuation within 1 cm for the upper X-point, but in the range of several centimetres away from the predefined reference point for the lower X-point in the vertical direction. In order for the X positions to be stably controlled with much lower fluctuations, the shape control has to be sufficiently consistent with the fast vertical position control. This remains to be fulfilled during the next experimental campaign.

3.2. LHCD experiments

The RF powers were applied in several ways. The LHW was used for current drive both in sustaining plasma discharges and assisting the plasma start-up. The ICRF was mainly applied for pre-ionization for reliable plasma start-up and wall conditioning in the last campaign. Most of these experiments were performed by pre-programming control of plasma shape and feedback control of current and position. The plasma shape and position were optimized to maximize the wave coupling into the plasma. Nearly 0.8 MW LHW at a fixed parallel refractive index $N_{\parallel}^{\mathrm{peak}} = 2.3$ has been successfully delivered, with ~0.65 MW power being coupled into the plasma, as shown in figure 12. The voltage variation $(V_{\mathrm{oh}} - V_{\mathrm{lh}})/V_{\mathrm{oh}} > 0.9$, indicating that this power can non-inductively sustain a 90% fraction of current at $I_{\mathrm{p}} = 250$ kA and a line-averaged density of $\sim 1.5 \times 10^{19}\,\mathrm{m}^{-3}$. The current driving efficiency deduced for full current drive at $V_{\mathrm{loop}} = 0$ from power scanning is about $0.8 \pm 0.1 \times 10^{19}\,\mathrm{A\,m^{-2}\,W^{-1}}$ under this condition, as shown in figure 13. It is nearly double the LHCD efficiency obtained in HT-7, but is smaller than that in Tore-Supra, mainly due to the lower volume averaged electron temperature in the present experiments. Significant electron heating by LHW has been observed both by soft x-ray pulse height analysis and XCS, while ion heating is very weak. Figure 14 shows the electron and ion temperature profiles derived from XCS for two LHCD discharges of 400 and 650 kW injection powers. Electron heating via collision between bulk electrons and fast electrons driven by LHW dominates in the plasma core, which implies the central power deposition of LHW, consistent with the code prediction.

Plasma discharges can be sustained over 20 s in such operation scenarios (figure 15). The main limitations for higher power and longer pulse are unstable coupling caused by plasma shape variations due to pre-programming shape control for LHCD plasma and the power supply stability of klystrons in the LHCD system. As shown in figure 15, the LHCD power was gradually decreased after 10 s mainly due to the power supply, which will be modified for the next campaign. The LHCD experiments were also performed at different plasma currents. Under the present conditions, LHCD can sustain plasma discharges of 400 kA and line-averaged density of $\sim 1.5 \times 10^{19}\,\mathrm{m}^{-3}$ for a duration of over 10 s. Maximum current drive efficiency up to $(1.0 \pm 0.1) \times 10^{19}\,\mathrm{Am^{-2}\,W^{-1}}$ has been achieved under this condition. This suggests that it is possible to sustain fully non-inductive plasma discharges at 500 kA and line-averaged density of $\sim 2.0 \times 10^{19}\,\mathrm{m}^{-3}$ with the presently

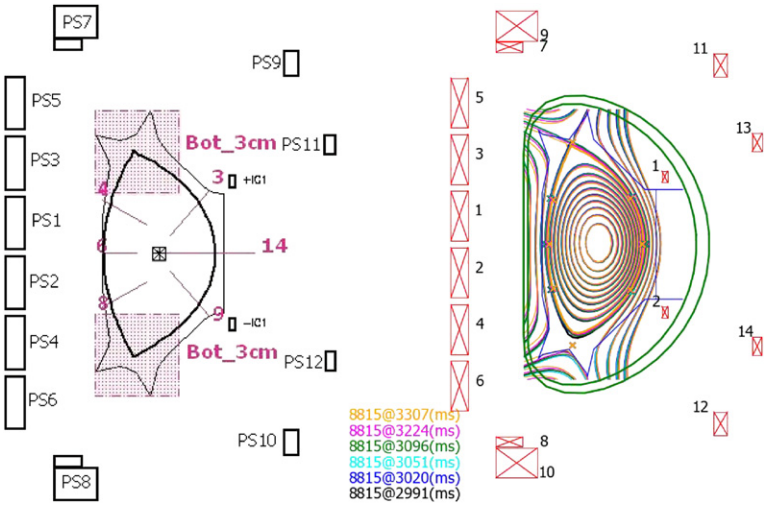

Figure 10. Left: reference point for iso-flux control, right: plasma shape controlled by iso-flux from 3 s at different time slices. The position fluctuation for top X point is within 1 cm, while several centimetres away from reference point for bottom X point.

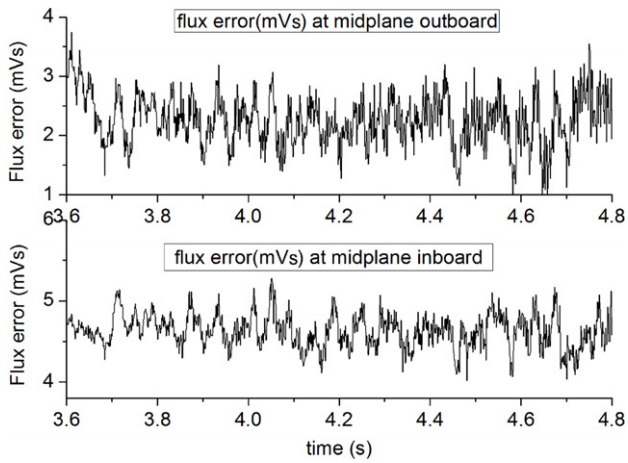

Figure 11. Flux errors at mid-plane outboard (top) and inboard (bottom) in the iso-flux control algorithm for the same shot as in figure 10.

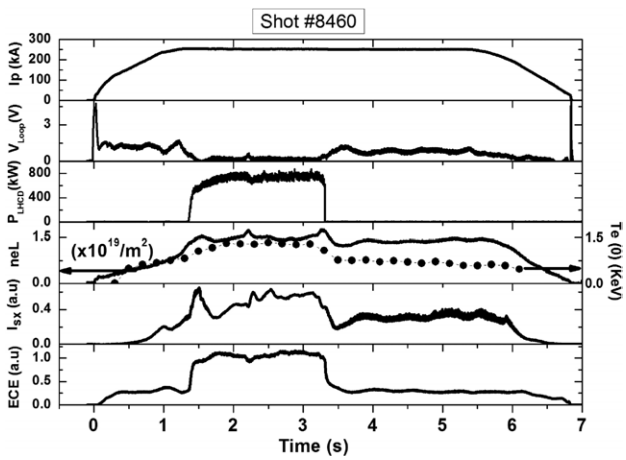

Figure 12. Delivered 800 kW LHCD power for nearly full non-inductive current drive. From top to bottom: plasma current, loop voltage, LHCD power, line integrated density (left axis) and electron temperature (right axis), intensity of SX emission in central sight line, ECE near plasma center.

available maximum LHW power of 2 MW, if plasma shape can be well controlled and the problem with the LHCD power supply is fixed.

3.3. Start-up of plasma discharges

Plasma initiation, ramp-up and control are very important issues for a full superconducting machine. The design allows the current varying rate in the PF magnets to be 20 kA s^{-1} for 60 ms and 10 kA s^{-1} for 160 ms within the safety margin for breakdown and initial plasma current ramp-up. Corresponding PF power supplies are specified to the limitation of current rate at 5 kA s^{-1}. Higher current rates are realized by initial magnetization of PF coils and then switching to resistors, which can provide higher voltage and is used only for breakdown and initial plasma current ramp-up. Full use of the PF capability can create a loop voltage of ~6.5 V with a reasonable null field configuration, which will produce vessel currents up to 150 kA [2] at breakdown and lead to a loss of poloidal magnetic flux of about 0.3 V s. Low loop voltage

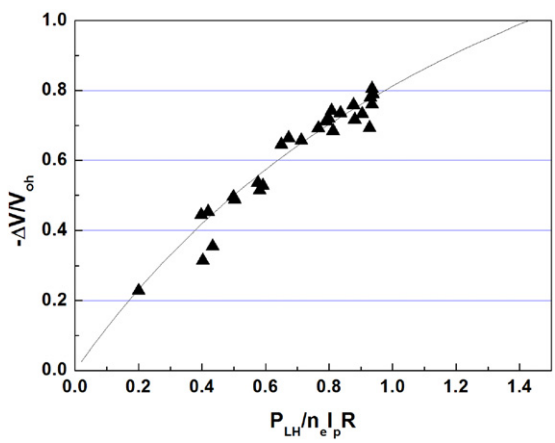

Figure 13. Normalized LHCD power versus variation of surface voltage for estimation of LHCD efficiency.

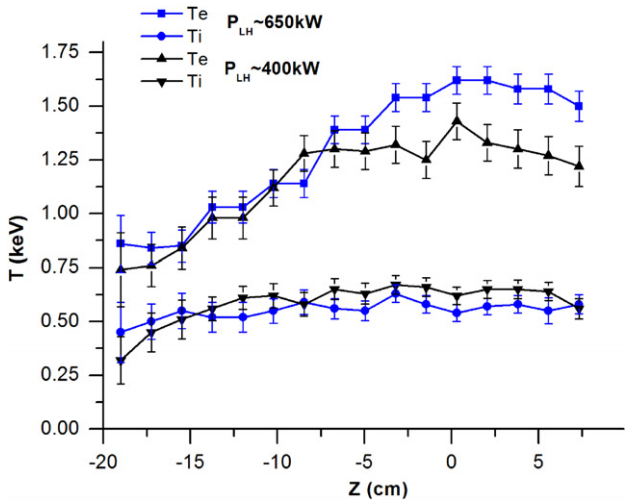

Figure 14. Electron and ion temperature profiles in two LHCD plasmas with powers of 400 kW and 650 kW, respectively.

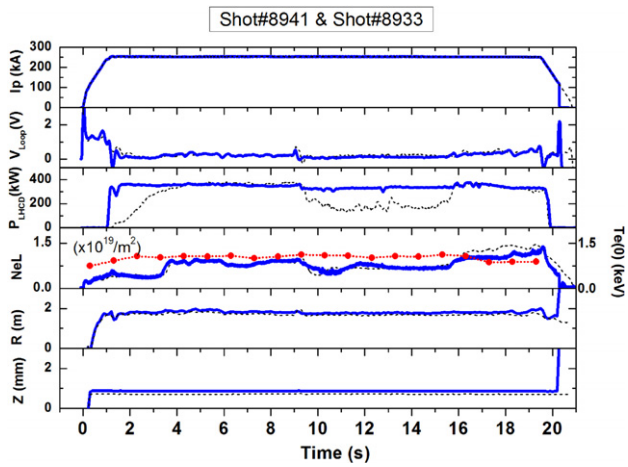

Figure 15. Long pulse discharge sustained by LHCD for 22 s. From top to bottom: plasma current, loop voltage, LHCD power, line integrated density and central electron temperature (dot for right axis), radial position and horizontal position of the plasma.

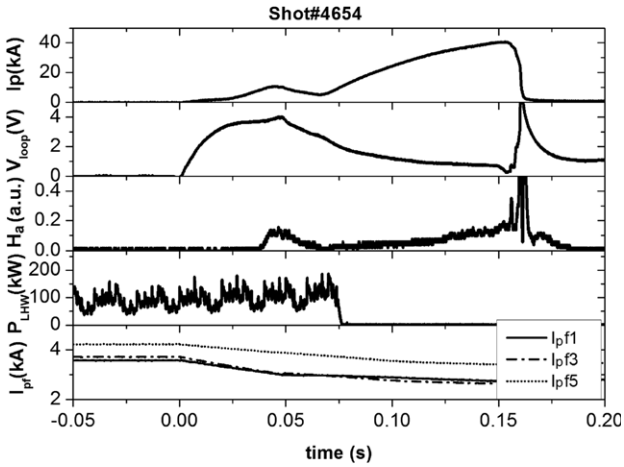

Figure 16. Low voltage start-up with assistance of LHW. From top to bottom: plasma current, loop voltage, Hα emission, LHW power, current in poloidal coils nos 1, 3, 5.

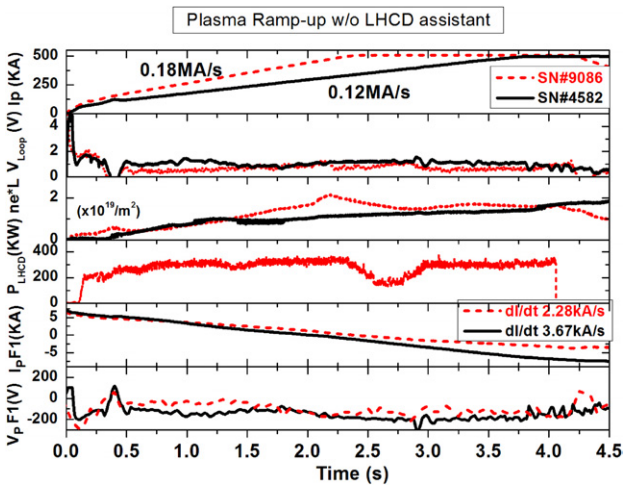

Figure 17. Plasma current ramp-up with (dashed curve) and without (solid curve) assistance of LHCD. From top to bottom: plasma current, loop voltage, line integrated density, LHW power, current and applied voltage on poloidal coil no 1.

start-up is beneficial not only for safety of machine operation but also for reducing the loss of poloidal magnetic flux due to vessel current.

Breakdown at a toroidal electric field of 0.3 V m^{-1} has been achieved by optimizing the null field configuration, gas pressure and assistance of the LHW of 100 kW and well conditioned wall. The result is shown in figure 16. The maximum current ramping rate in PF coils is 10 kA s^{-1} with a voltage applied on PF coils only half of the normal operational voltage for breakdown, which increases the safety margin of PF coils significantly. At the same time, the loss of poloidal magnetic flux due to vessel current (<100 kA) is only 0.1 V s.

A very low plasma ramp rate of 0.12 MA s^{-1} during the plasma current ramping up phase has been obtained under well boronized wall conditions. Such a low ramping rate enabled the operation of the PF coils and power supplies in the region far from their limits. However, plasma current ramping at such a low rate was not always reliable due to burn through at low temperatures. Applying LHCD during the plasma start-up phase can significantly reduce the current ramping rate in PF coils or the voltage applied to PF coils for the same plasma current ramping rate. On the one hand, operation mode minimized the heat deposition on the PF coils caused by ac losses, and hence increased the safety of machine operation. On the other hand, it allows better plasma control, particularly during the shaping phase due to the larger voltage regulation margin of PF power supply. Typical results with and without LHCD applied during the start-up are compared in figure 17. It is clearly shown that both the current ramping rate and the voltage applied to PF coils were significantly reduced with the assistance of LHCD, although the plasma current ramping rate was higher with LHCD. The main issue with applying the LHCD during the start-up phase is the optimization of coupling to launch the power into the plasma.

3.4. Physical engineering effects

In the case of frequent variation of the plasma performance such as large ELM burst and monster sawteeth, the PF currents need to be adjusted to maintain the plasma equilibrium and

keep the configuration. For typical EAST plasmas at a current of 500 kA, the maximum PF current variation of about 300 A estimated by EFIT is needed to keep the configuration if the poloidal beta is changed by 10%. This will cause a continuous PF coils current varying rate of 3 kA s^{-1}, if this beta variation is led by a sawtooth with a typical period on the 0.1 s scale in EAST. Continuous heat deposition caused by ac losses on the PF coils can limit the pulse length of the discharge when the magnet temperature could not be maintained below the marginal value at a certain cooling power. In this case, the cooling power has to be increased to keep the magnet temperature within the safety margin. Therefore, effects of plasma discharge and operation scenarios on the superconducting magnets, particularly on the PF magnetic system and the cryogenic system, pose constraints for future steady-state operation of a superconducting machine.

These issues have been investigated by simulating discharges or during plasma discharges. Plasma disruption does not seem to be a direct safety constraint for superconducting PF coils due to the strong shielding effect from the vacuum vessel, as inductive voltages on the PF coils due to disruption are low [2]. But such an algorithm has to be adopted in controlling the PF current ramping down rates after the termination of the plasma discharge to avoid higher thermal load on the magnets and cryogenic system. The energy deposition on TF coils, TF cases and PF coils due to the ac losses caused by varying PF currents has been investigated at different current ramping rates for a sufficient duration up to the saturation of the outlet liquid helium temperature in the PF coils. Figure 18 shows an example for the outlet temperature rise of the CS during the excitation at a constant rate of 1 kA s^{-1} in triangular waveforms of the PF current. The temperature rise seems to be saturated for a sufficient excitation duration and is still below the safety margin of 1 K. Keeping the magnet temperature below the safety margin at a higher PF current variation rate requires more cooling power. The capability of the present cryogenic system on EAST is sufficient to keep the magnet temperature and coolant helium pressure much lower than the marginal values if the current varying rates in PF coils do not exceed the designed specification. More issues about safety operation for superconducting magnets have been discussed elsewhere [13].

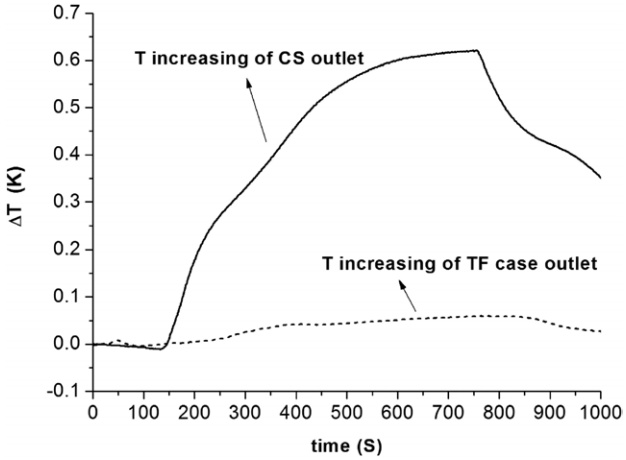

Figure 18. Outlet temperature rise of CS (solid line) and case of toroidal coils (dashed line) at excitation rate of 1 kA s^{-1}.

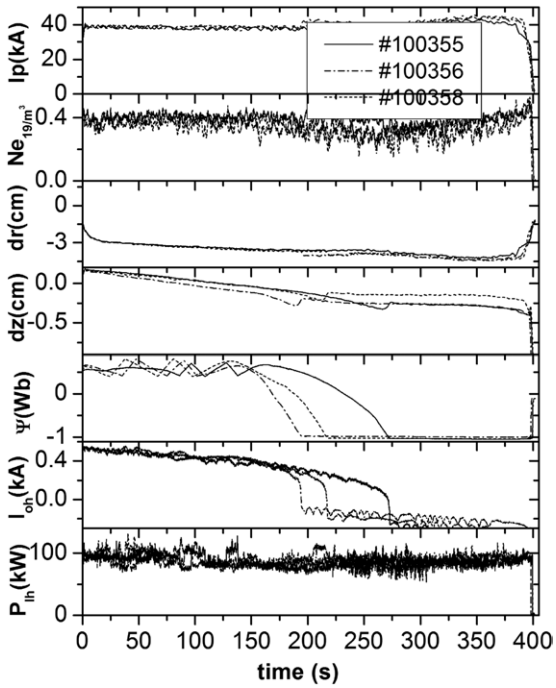

Figure 19. Repeatable long pulse discharges for 400 s. From top to bottom: plasma current, line-averaged density, radial position, vertical position, magnetic swing flux of transformer, current in CS and LHCD power.

4. Experiments in HT-7

Since the last IAEA meeting, the experiments on the HT-7 tokamak have focused on long pulse discharges under different scenarios and high power heating to support EAST experiments both physically and technically. To meet the long pulse operation requirements, several systems on HT-7 have been modified. The plasma control algorithm was implemented based on real-time magnetic equilibrium reconstruction with improved magnetic diagnostics. The iron core is simplified by using the 'spool' model [14] and gaps of the last closed flux surface from the PFCs are adopted for the plasma control. New heat sink technology and materials were utilized to replace the belt limiter at the high field side (HFS) for validation and supporting construction of the EAST in-vessel components.

4.1. Long pulse discharges

Long pulse experiments were performed by driving the plasma current fully non-inductively through the use of LHCD, which was realized in two different scenarios. The first one is via feedback control of the magnetic swing flux of the transformer at a constant. The second way is so-called transformer-less discharges, which was realized by over current drive up to reversed saturation of the transformer and then switching off the current in the central solenoid. Experimental observation by hard x-ray pulse height analysis indicates that the cut-off energy of supra thermal electrons is smaller in the transformer-less discharges than in the first scenarios. These techniques have been used successfully to sustain the plasma discharges

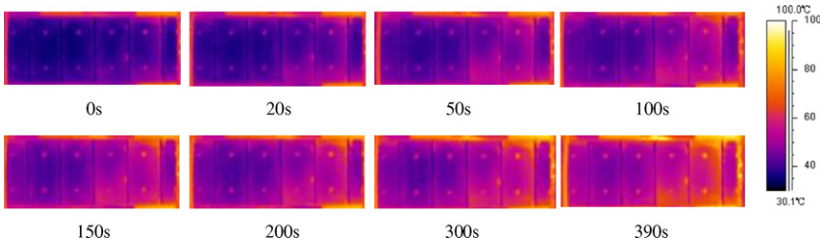

Figure 20. Surface temperature of the belt limiter in the HFS. The toroidal range shown in the figure is about 42°.

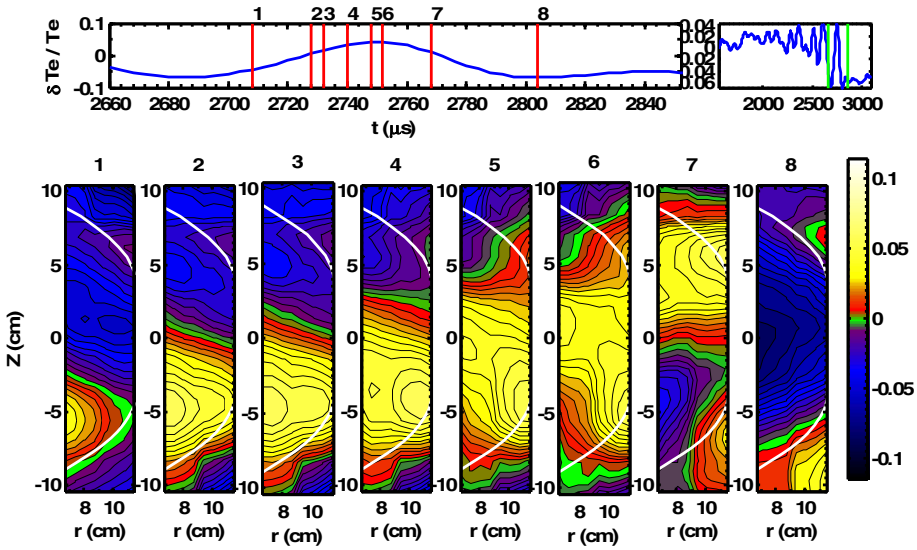

Figure 21. The 2D image of temperature fluctuation evolution during the reconnection process at LFS (bottom plot). The inversion radius shown as the white line is determined from the assumption that fluctuation is most quiet near the inversion radius (#93513, about 537 ms). The right top plot shows a period of sawteeth crash observed by one channel of ECEI. The left top plot shows the crash time interval indicated by two vertical green lines in the right top plot. Time slices for 2D image are also indicated in this plot.

for 400 s at $I_p \sim 50$ kA, as shown in figure 19, which set the new record in HT-7. The magnetic flux of the transformer was controlled at a constant during the first 150 s in these three shots. Then, over current drive led to switching off the central solenoid at about 200 s, 210 s and 270 s, respectively. There were no observable hot spots during the transformer-less discharges, which might be correlated with the disappearance of further acceleration of fast electrons driven by LHCD. In such an operation mode, the surface temperature of the belt limiter could be well controlled below a certain value for the entire plasma discharge duration as shown in figure 20. These long pulse experiments indicate the success of the newly built belt limiter, and more importantly, validate the same heat sink material and structure used for the EAST PFCs. The well controlled surface temperature also suggests an important role of supra thermal electrons on the heat load on the limiter. The limitation for even longer pulse is from uncontrollable density rise caused by out-gassing mainly from the first wall, which was heated by plasma radiation without active cooling.

4.2. Sawteeth investigation

Sawtooth oscillation is one of the most important MHD instabilities in tokamaks. Recently, progress has been achieved by using newly developed 2D ECE imaging (ECEI) and high-resolution soft-x-ray multi-arrays to verify new models [15, 16]. There are five high-resolution soft-x-ray arrays and a 2D ECEI system consisting of 8 (radial) × 16 (vertical) channels on HT-7 for the investigation of sawtooth activity and temperature turbulence. The resolution of ECEI is about 1 cm (radial) × 1.1 cm (vertical) per pixel. ECEI covers a region of about 5 cm (radial) × 20 cm (vertically symmetric along mid-plane) in a poloidal cross-section. The time resolution is about 4 μs with a noise to signal level of about 1%. The high-resolution soft-x-ray arrays are located in one poloidal cross-section with different poloidal view angles, with 46 channels in each array, covering the whole plasma region.

The islands coalescence was observed by the 2D ECEI system in ohmic plasmas with $B_t = 1.9$ T, $I_p = 170$ kA and a central line-averaged density of 2.4×10^{19} m^{-3} before reconnection during the $m = 1$ sawtooth crash. A representative view of the sequence of 2D ECEI images during the reconnection process is shown in figure 21. At the top of the figure, a time history of the temperature fluctuation measured by one of the 128 channels (inter) illustrates the typical precursor oscillations and crash process. The reconnection that takes place on the $q = 1$ radius in the low field side (LFS) makes the magnetic field line open. As a result, the heat flow escapes to the outside of the inversion radius collectively. Similarly, magnetic reconnection is also found by 2D imaging of the HFS. The characteristic of magnetic

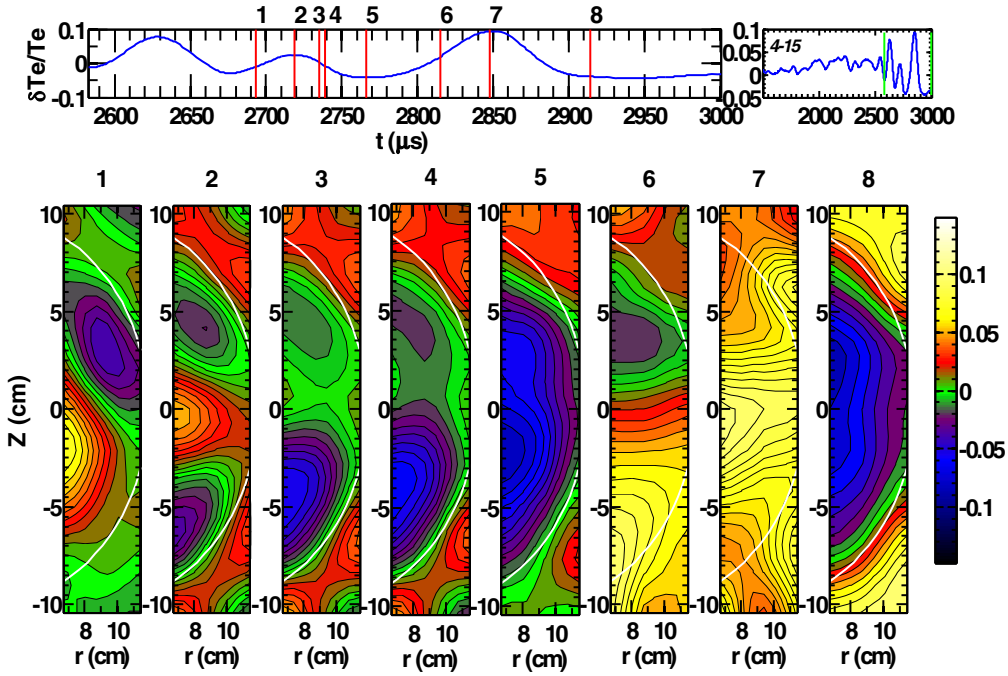

Figure 22. The evolution of $m = 2$ mode islands coalescence before sawtooth crash (#93513, about 525 ms). The right top plot shows a period of sawteeth crash observed by one channel of ECEI. The left top plot shows the crash time interval indicated by two vertical green lines in the right top plot. Time slices for 2D image are also indicated in this plot.

reconnection near inversion radius during sawtooth oscillation is analogous to that observed on TEXTOR [15].

Figure 22 shows the evolution of the $m = 2$ islands coalescence on the $q \sim 1$ surface during the precursor phase of sawteeth. The first island rotates anticlockwise passing through the diagnostic region in frames 1 and 2. The island can still be seen in the diagnostic region in the subsequent frame, while simultaneously another island rotates into the diagnostic region below. The two islands reconnect near the mid-plane in only about 10 μs, as shown in frames 3 and 4, and finally, the two islands coalesce into one island as the $m = 1$ mode in frame 5. After the formation of the $m = 1$ island, the heat in the core escapes to the outside of the inversion radius during sawtooth crash during frames 6 to 8.

The ECEI clearly presents the characteristics of the temperature fluctuation during the sawtooth crash phase. However, observation is limited by a relatively small spatial region. Tomography of high-resolution soft-x-ray arrays can give the sawtooth crash structure. The Fourier–Bessel inversion method is used in the reconstruction by choosing $M = 2$–3 and $L = 6$–8 [16]. In order to see the structure of the crash process more clearly, the sawtooth activity in LHCD plasma is analysed due to the large fluctuating amplitude (20–30% of the total emission in the central sightline) for distinguishing the crash and precursor stages. In order to obtain the picture of plasma pressure variation (hence heat flow) due to sawtooth oscillations, the singular value decomposition (SVD) technique is employed to extract the perturbation components from the signals. The reconstruction with only perturbation signals, which reflects the variation of plasma pressure caused by the oscillations in the plasma, can show the mode structure very distinctly.

By using this method, the reconstructed sawtooth crash process from perturbation signals of a sawtooth crash is shown in the bottom frames in figure 23. The top row of the figure shows the evolution of the soft-x-ray signals, where the markers from A–F correspond to the time slices for reconstruction. The middle row shows the topography from the total signals, and the bottom row shows the contour plot of the reconstructed perturbation signals extracted by the SVD method. At time slice C, particularly from the contour plot of the reconstructed perturbation signals in the bottom row, it is clearly seen that the $m = 1$ (red part) and $m = 2$ (blue part) islands were formed. It shows that a large heat flow transfers across the X point of both the $m = 1$ and $m = 2$ islands from time slices C–E, then the transferred energy gradually spreads poloidally over the peripheral region near the $q = 1$ surface (E–F), while the reconstructed sawtooth crash process from the total signals, as shown in the middle frames in figure 23, seems to be consistent with Kadomtsev's model, which was also concluded in [15]. Asymmetric heat flow can occur in both LFS and HFS, which is different from the observations in high β plasmas on TFTR [17]. The heat flow characteristics near the X point during the sawtooth crash phase are consistent with the observations from 2D ECEI. Another type of sawtooth crash is shown in figure 24, where the heat flow transfer is not across the X point of the $m = 1$ island, but across one of the X points of the $m = 2$ magnetic islands instead (this mode is rather weak but can be identified) as indicated by the arrow in the right bottom plot. This suggests that the large $m = 1$ component in the soft-x-ray signals is due to the large asymmetric heat flow during the sawtooth crash phase rather than the abruptly increasing $m = 1$ magnetic island. Another interesting observation is shown in figure 25. The heat flow transfers across both X points of the $m = 2$ magnetic islands indicated by the arrows in the right bottom plot, with little asymmetry in LFS and HFS. In this example, the X point of

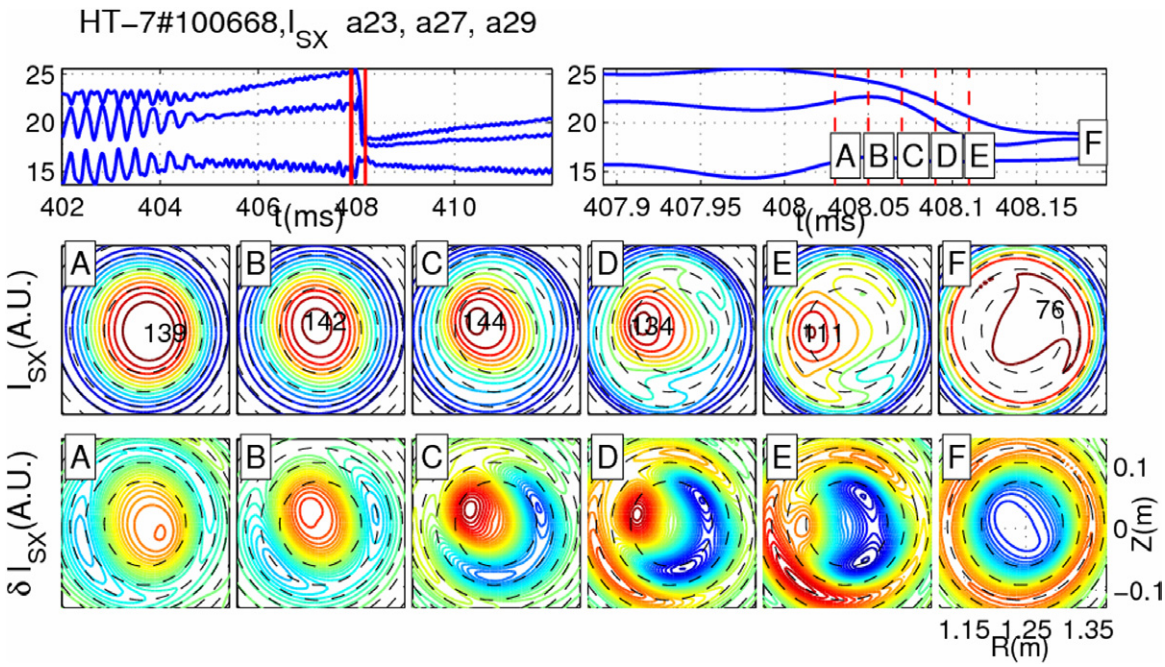

Figure 23. Reconstructed sawtooth crash picture by topography. The top row shows the evolution of the soft-x-ray signals. The middle row is topography from total signals, and the bottom row is the contour plot of the reconstructed perturbation signals extracted by the SVD method.

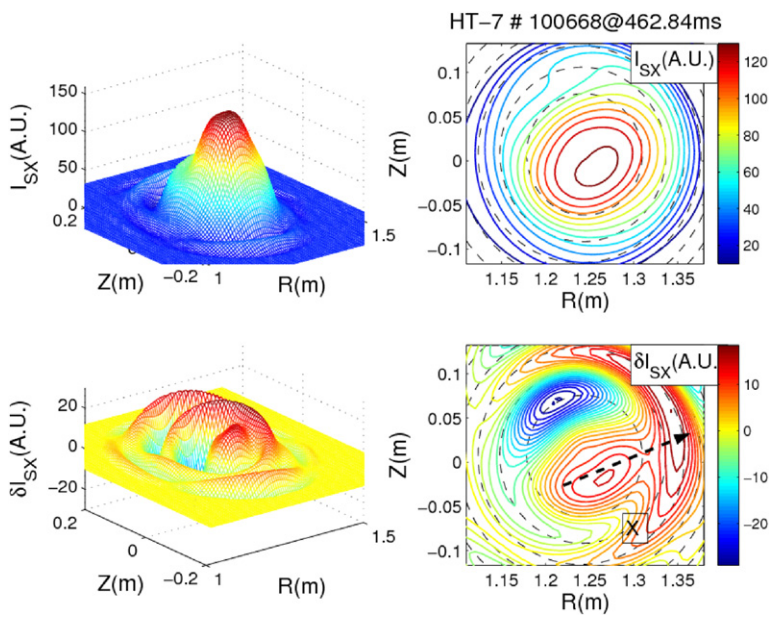

Figure 24. Reconstructed soft-x-ray profile during sawtooth crash by topography. The top frames are reconstructed from total signals and the bottom frames from perturbative signals.

the $m = 1$ islands is overlapped with one of the O points of the $m = 2$ magnetic islands, which can be identified by the asymmetry of the two O points of the $m = 2$ magnetic islands. This result again demonstrates that the sawtooth crash is not caused by the fast reconnection of the $m = 1$ magnetic island.

The observation above strongly suggests that the sawtooth crash is not caused by the fast reconnection of the $m = 1$ magnetic island, while the picture is in agreement with the turbulence model [18]. For the turbulence model, the large heat flow and hence the crash are the result of the fast energy and particle diffusion in the magnetic stochastic region around the separatrix of the magnetic islands. More detailed analysis and discussion will be published in the journal of Plasma Physics and Controlled Fusion.

4.3. Turbulence measurements

Both the electron mode and the ion mode coexisting in high density ohmic plasmas with $\bar{n}_e \geqslant 4.5 \times 10^{19}\,\mathrm{m}^{-3}$ have been observed by 2D ECEI. The local wavenumber–frequency spectrum obtained by the two-points correlation technique is

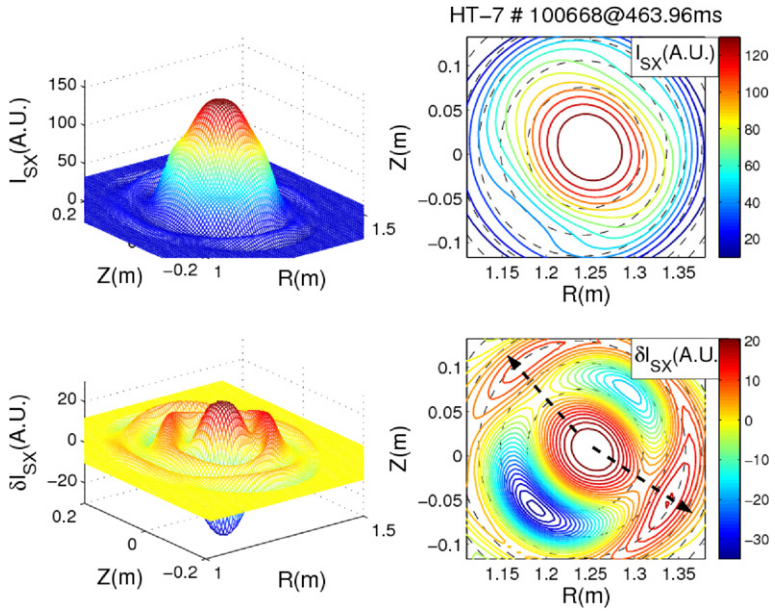

Figure 25. Reconstructed soft-x-ray profile during sawtooth crash by topography. The heat flow transfer across both the X points of the $m = 2$ island can be identified in the bottom frame.

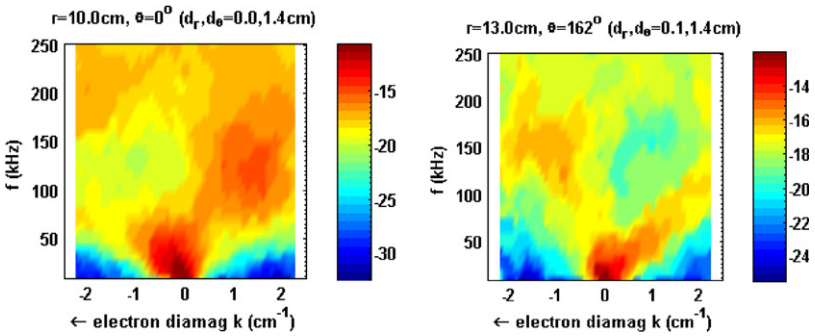

Figure 26. The wavenumber–frequency spectra of temperature fluctuation at LFS (left) and at HFS (right).

shown in figure 26. The two modes are found to coexist at $r \sim 10$ cm in the LFS and $r \sim 13$ cm in the HFS. The ion temperature gradient mode in the density fluctuation was observed by far-infrared (FIR) scattering and beam emission spectrum (BES), but has not been reported in the temperature fluctuation yet. Further experiment and analysis are needed to clarify this observation, which will be discussed in detail in a separate paper.

Since there are two windows located at the top of the machine separated by 120° toroidally for the Langmuir probes, the long-distance correlational potential structure could be detected in both poloidal and toroidal directions. The experiments were carried out in high q_a (6.6–8.5) plasmas with a line-averaged density of (1–2) $\times 10^{19}$ m^{-3}. The poloidal and toroidal mode numbers from the floating potential fluctuations have been measured to be far below one at 1–12 kHz. The central frequencies of the geodesic acoustic mode (GAM) are around 12 kHz. The radial wavenumber–frequency spectrum $S(k_r, f)$ of the GAM has been estimated from the floating potential fluctuations of radially separated tips of the Langmuir probes. The spectral averaged wavenumber and spectral width are, respectively, $\bar{k}_r = 0.83\,\mathrm{cm}^{-1}$ and $\Delta k_r = 4.6\,\mathrm{cm}^{-1}$, corresponding to $k_r\rho_i \sim 0.065$ and $\Delta(k_r\rho_i) \sim 0.31$. These are in the range for the GAM expected by theory [19] and simulation [20] and consist of the experimental results in other devices [21]. Further discussion is beyond the scope of this paper.

5. Summary and near future plan

Since the last IAEA meeting, significant progress has been made in the construction of fully actively water cooled in-vessel components and plasma control to achieve highly shaped plasmas on EAST. The primary achievements, particularly the experiences from the last two years, provide us with confidence that the highly shaped plasma with relevant performance could be sustained by RF for long durations, although some improvements are needed for reliable machine operation.

Presently, a 2 MW LHCD system at 2.45 GHz and a 1.5 MW ICRF system at 30–110 MHz are in operation. A new ICRF system with the maximum output power of 4.5 MW at 25–70 MHz will be available in 2009. A new ICRF antenna array will be designed and manufactured with phasing capability. The present LHCD system is planned to be upgraded to 4 MW, where the existing klystron of 100 kW will

be replaced by a new klystron of 200 kW. The capability of the corresponding power supplies and water cooling, etc will be expanded within the next 2 years. The total RF heating and current drive power will be 10 MW in CW by the end of 2010. This is much higher than the H-mode threshold, which is about 4 MW for the standard EAST operation scenario at 1 MA plasma current and toroidal field of 3.5 T. The flexibilities of heating scenarios and current drive in controlling power deposition and current density profiles provide the possibilities to operate EAST in high performance regimes with edge and/or internal transport barrier, which allow investigation to be focused on advanced scenarios for long pulse. A new proposal for a 4 MW LHCD system at 4.6 GHz and a 2–4 MW neutral beam injection system at 50–80 keV has been approved for the next 4 years.

In the next two years, the diagnostics system on EAST will be further extended to provide measurements of all key profiles, including Thomson scattering for density and electron temperature, charge exchange recombination spectroscopy based on a diagnostic beam for ion temperature and rotation, bolometry for radiation power, x-ray crystal spectroscopy for ion/electron temperature and plasma rotation velocity, multi-channel ECE or 2D ECE image for electron temperature and fluctuation, visible bremsstrahlung for effective charge number, multi-channel DCN laser interferometer for density, HX-ray arrays for LHW-driven fast electron bremsstrahlung, neutral particle analyzer for energetic particles, optical and spectroscopic diagnostics for impurity, etc. Some of them will be built via international collaboration. These diagnostics should be sufficient to describe the basic plasma performance and provide input for integrated modelling and data analysis.

HT-7 will still be operated before EAST is equipped with sufficient heating and current drive capability and diagnostics. Future experiments on HT-7 will focus on the issues related to plasma and wall interactions under long pulse conditions and some specific topics, such as MHD instabilities, transport and turbulence by Langmuir probes, newly developed CO_2 laser scattering and 2D ECE image systems.

Acknowledgments

This work was supported by the National Natural Science Foundation of China under Grant Nos 10725523 and 10721505, and partially supported by the Core-University Program of Japanese Society of Promote Sciences.

Appendix

EAST and HT-7 Teams

Baonian Wan[1], Jiangang Li[1], Yuanxi Wan[1], Xianzhu Gong[1], Bingjia Xiao[1], Peng Fu[1], Yuntao Song[1], Yu Wu[1], Jiafang Shan[1], Yanping Zhao[1], Liqun Hu[1], Liman Bao[1], Yanfang Bi[1], Lei Cao[1], Jiafeng Chang[1], Junling Cheng[1], Xu Deng[1], Bojiang Ding[1], Jiayi Ding[1], Siye Ding[1], Shijun Du[1], Yanmin Duan[1], Jia Fu[1], Daming Gao[1], Ge Gao[1], Wei Gao[1], Xiang Gao[1], Zhe Gao[4], Shiying He[1], Liansheng Huang[1], Zhensan Ji[1], Yinxian Jie[1], Guiming Li[1], Shiyao Lin[1], Bili Ling[1], Adi Liu[5], Dongmei Liu[1], Fukun Liu[1], Guangnan Luo[1], Jiarong Luo[2], Zhengping Luo[1], Dengkui Ma[1], Yuzhou Mao[1], Shengming Pan[1], Wanjiang Pan[1], Jing Qian[1], Jinping Qian[1], Chengming Qing[1], Pinjian Qing[1], Biao Shen[1], Linhai Sheng[1], Xiaoyang Sheng[1], Yuejiang Shi[1], Youwen Sun[1], Ang Ti[1], Xiaogang Wan[1], Huazhong Wang[1], Linsen Wang[1], Mao Wang[1], Keping Wu[1], Hao Wu[1], Jiefeng Wu[1], Junshuan Wu[1], Songtao Wu[1], Weiyue Wu[1], Yichun Wu[1], Zhenwei Wu[1], Weibing Xi[1], Chunyi Xie[1], Guosheng Xu[1], Liuwei Xu[1], Ping Xu[1], Tiejun Xu[1], Xiaoyuan Xu[5], Diye Xue[1], Lei Yang[1], Li Yang[1], Qingwei Yang[3], Zhongshi Yang[1], Chanxuan Yu[5], Chunyan Yuan[1], Qiping Yuan[1], Junyu Zhao[1], Qing Zhan[1], Qiyong Zhang[1], Wei Zhang[1], Xiaodong Zhang[1], Xinjun Zhang[1], Guanghua Zhen[1], Fali Zhong[1], Guoqiang Zhong[1], Yanfei Zhu[1], Youhua Zhu[1], Ping Zhu[1], Ming Zhuang[1]

International Collaborators

Paul Anderson[6], Vincent Chan[6], Dave Humphreys[6], Al Hyatt[6], R. Johnson[6], Lang L. Lao[6], Jim Leuer[6], Ali Mahdavi[6], Gary Jackson[6], Ben Penaflor[6], David Piglowski[6], Michael Schaffe[6], Mike Walker[6], Anders Welander[6], He Huang[7], Kenneth Gentle[7], Perry Philippe[7], William Rowan[7], D. Mueller[8], M. Bitter[8], K.W. Hill[8], D.M. Mastrovito[8], Houyang Guo[9], R. Kumazawa[10], T. Mutoh[10], K. Saito[10], T. Watari[10], B. Bremond[11], K. Vueillie[11], S.G. Lee[12], J.G. Bak[12]

[1] Institute of Plasma Physics, Chinese Academy of Sciences, Hefei, People's Republic of China
[2] Donghua University, Shanghai, People's Republic of China
[3] South West Institute of Physics, Chengdu, People's Republic of China
[4] Tsinghua University, Beijing, People's Republic of China
[5] University of Science and Technology of China, Hefei, People's Republic of China
[6] General Atomic, San Diego, USA
[7] Fusion Research Center, UT at Austin, USA
[8] Princeton Plasma Physics Laboratory, USA
[9] Tri Alpha Energy, California, USA
[10] National Institute for Fusion Sciences, Toki, Japan
[11] Association Euratom-CEA, CEA Cadarache, France
[12] Natiaon Fusion Research Institute, Korea Basic Science Institute, Daejeon, Korea

References

[1] Wan Y. *et al* 2006 Overview progress and future plan of EAST Project *Proc. 21st Int. Conf. on Fusion Energy 2006 (Chengdu, China, 2006)* (Vienna: IAEA) CD-ROM file OV/1-1 and http://www-naweb.iaea.org/napc/physic/FEC/FEC2006/html/index.htm
[2] Wan B. *et al* 2006 First plasma in EAST *Proc. 21st Int. Conf. on Fusion Energy 2006 (Chengdu, China, 2006)* (Vienna: IAEA) CD-ROM file PD/P6-5 and http://www-naweb.iaea.org/napc/physic/FEC/FEC2006/html/index.htm
[3] Wan B. *et al* 2003 *Nucl. Fusion* **43** 1279
[4] Wan B. *et al* 2005 *Nucl. Fusion* **45** S132
[5] Wan B. *et al* 2003 *J. Nucl. Mater.* **313–316** 127–34
[6] Bitter M. *et al* 1999 *Rev. Sci. Instrum.* **70** 292
[7] Lee S.G. *et al* 2004 *Rev. Sci. Instrum.* **75** 3693
[8] Xiao B.J. *et al* 2008 EAST plasma control system *Fusion Eng. Des.* **83** 181–7

[9] Kuang G. *et al* 1999 *Fusion Technol.* **36** 212
[10] Lao L.L. *et al* 1985 *Nucl. Fusion* **25** 1611
[11] Bracco G. and Thomsen K. 1997 *Nucl. Fusion* **37** 759
[12] Ferron J.R. *et al* 1998 *Nucl. Fusion* **38** 1055
[13] Yuanxi Wan *et al* 2008 Risk analyses and optimization of safe operation for advanced superconducting tokamak *Proc. 22nd Int. Conf. on Fusion Energy 2008 (Geneva, Switzerland, 2008)* (Vienna: IAEA) CD-ROM file FT/P3-24 and http://www-naweb.iaea.org/napc/physic/FEC/FEC2008/html/index.htm
[14] Solano E.R. *et al* 1990 *Nucl. Fusion* **30** 1107
[15] Park H.K. *et al* 2006 *Phys. Rev. Lett.* **96** 195004
[16] Janichi C. *et al* 1989 *Phys. Rev. Lett.* **62** 3038
[17] Nagayama Y. *et al* 1996 *Phys. Plasmas* **3** 1647
[18] Lichtenberg A.J. 1984 *Nucl. Fusion* **24** 1277
[19] Diamond P.H. *et al* 2005 *Plasma Phys. Control. Fusion* **47** R35
[20] Hahm T.S. *et al* 2000 *Plasma Phys. Control. Fusion* **42** A205
[21] Fujisawa A. *et al* 2007 *Nucl. Fusion* **47** S718